The International Journal of Advanced Manufacturing Technology (2019) 105:2891–2906
https://doi.org/10.1007/s00170-019-04417-3

ORIGINAL ARTICLE

Multi-Laser Powder Bed Fusion Benchmarking—Initial Trials with Inconel 625

H. Wong [1] · K. Dawson [1] · G. A. Ravi [2] · L. Howlett [2] · R. O. Jones [2] · C. J. Sutcliffe [1,2]

Received: 3 June 2019 / Accepted: 12 September 2019 / Published online: 9 November 2019
© The Author(s) 2019

Abstract

Production rate is an increasingly important factor in the deployment of metal additive manufacturing (AM) throughout industry. To address the perceived low production rate of metal AM systems based on single-laser powder bed fusion (L-PBF), several companies now offer systems in which melting has been parallelised by the introduction of multiple, independently controlled laser beams. Nevertheless, a full set of studies is yet to be conducted to benchmark the efficiency of multi-laser systems and, at the same time, to verify if the mechanical properties of components are compromised due to the increase in build rate. This study addresses the described technology gaps and presents a 4-beam L-PBF system operating in "single multi" (SM) mode (SM-L-PBF) where each of the four lasers is controlled so that it melts all of a particular components' layers and produces specimens for comparison with standard L-PBF specimens from the same machine. That is all four lasers making all of some of the parts were compared to a single-laser manufacturing all of the parts. Build parameters were kept constant throughout the manufacturing process and the material used was Inconel 625 (IN625). Stress-relieving heat treatment was conducted on As-built (AB) specimens. Both AB and heat-treated (HT) specimen sets were tested for density, microstructure, tensile strength and hardness. Results indicate that the stress-relieving heat treatment increases specimen ductility without compromising other mechanical properties. SM-L-PBF has achieved a build rate of 14 cm^3/h when four 200 W lasers were used to process IN625 at a layer thickness of 30 μm. An increase in the build rate of 2.74 times (build time reduction: 63%) has been demonstrated when compared to that of L-PBF, with little to no compromises in specimen mechanical properties. The observed tensile properties exceed the American Society for Testing Materials (ASTM) requirements for IN625 (by a margin of 22 to 26% in the 0.2% offset yield strength). Average specimen hardness and grain size are in the same order as that reported in literatures. The study has demonstrated that a multi-laser AM system opens up opportunities to tackle the impasse of low build rate in L-PBF in an industrial setting and that at least when operating in single mode there is no detectable degradation in the mechanical and crystallographic characteristics of the components produced.

Keywords Additive manufacturing · Multi-laser powder bed fusion · Selective laser melting · Mechanical properties · Inconel 625

1 Introduction

Advances in material discovery and efficient manufacturing are essential to the continued adoption of any new manufacturing technology. In order to secure the future of new innovations, methods which enable speedy material development, with minimum waste and post-processing combined with a reduced cost must be developed. Against this

✉ H. Wong
hay.wong@liv.ac.uk

K. Dawson
kdaws@liverpool.ac.uk

G. A. Ravi
Ravi.Aswathanarayanaswamy@Renishaw.com

L. Howlett
Laura.Howlett@Renishaw.com

R. O. Jones
Rhys.Jones2@Renishaw.com

C. J. Sutcliffe
cjs1@liverpool.ac.uk

[1] School of Engineering, University of Liverpool, Liverpool L69 3GH, UK

[2] Renishaw Additive Manufacturing Product Division, Stone, Staffordshire ST15 0SH, UK

backdrop, additive manufacturing (AM) has been identified as a disruptive manufacturing technique for the production of net-shape metallic components [1]. Whilst traditional manufacturing methods, such as machining and casting, will remain important, AM offers many advantages in terms of design freedom and material economy. Selective laser melting (SLM) or laser powder bed fusion (L-PBF) is one of the metal AM techniques beginning to achieve production uptake. L-PBF is a metallic powder bed, laser-driven, layer-by-layer process which utilises a scanning galvanometer system to divert a process laser across a metallic powder bed in order to create complex 3D components [2]. Despite the perceived benefit of L-PBF, there is, however, an impasse due to the low build rate [3] owing to the scanning mirror inertia in the galvanometer [2]. Electron beam melting (EBM) is another metal AM technique [4] posing a threat to the continued adoption of commercial L-PBF. This technology has a major advantage in scan speed due to the utilisation of massless electromagnetic lenses to manipulate a material-processing electron beam [4]. This enables the EBM process to have a build rate in the region of 80 cm^3/h [1], which is currently beyond the reach of any L-PBF system (single 200 W laser SLM typical build rate, 5cm^3/h [1]).

Multi-laser processing has been reported before, for example, by Andani et al [5] when the team investigated spatter formation, and by Li et al [6] when his group studied the microstructure and mechanical properties of Ti-6Al-4V components fabricated by multi-laser melting. However, experiments are yet to be carried out to quantify the effectiveness of multi-laser systems and, at the same time, to investigate if the mechanical properties of specimens are compromised due to the increase in build rate. This study aims to address the described research gaps and present a study involving a multi-laser L-PBF system for the processing of Inconel 625 (IN625). The system is designed to improve the speed and build efficiency of L-PBF systems to compete with the production speed of EBM whilst maintaining the mechanical and microstructural properties of components. The multi-laser system offers numerous advantages over the current crop of available L-PBF systems. If multi-laser L-PBF is to be an industrially acceptable process capable of the manufacture of regulated components, then effects caused by the use of multiple laser sources on component mechanical properties must be understood. This paper investigates the effect of using multiple laser beams for L-PBF. A 4-beam system was used to produce specimens from IN625 powder with a layer thickness of 30 μm. Stress-relieving heat treatment was conducted to relieve thermal residual stress on as-built (AB) specimens. Both AB and heat-treated (HT) specimen sets were tested for density, hardness, tensile strength and microstructure. Single-laser specimen test results were compared to multi-laser results to investigate any influence from the use of multiple laser sources on mechanical properties.

2 Materials and Methods

This section describes the materials and methods used in this study in the following order: equipment; L-PBF laser beam arrangements; specimen type; powder properties; process optimisation method; heat treatment; mechanical testing conditions.

2.1 Manufacturing Equipment

Specimens were manufactured using a L-PBF and a prototype SM-L-PBF machine. The prototype machine has the same basic configuration as a RenAM500Q (Renishaw, UK). The machine has four individually controlled beam paths with 500 W modulated laser light at 1070 nm. Galvanometer scanners are provided in each channel with each scanner being inserted into a water-cooled aluminium housing. This housing provides consistent cooling, maximising the pointing stability of each laser channel. The light is delivered through an active (no f-theta) focusing system to the powder bed ensuring consistent 80 μm spot size over the 250 mm × 250 mm build area. A point-based exposure strategy is used with a maximum modulation rate of 25 k Hz (minimum exposure time is 40 μs) with a 10-μs resolution. Inert gas shielding is provided by vacuum swing inert monitored to an accuracy of ± 10 ppm. Gas filtering is performed using a dual-filter paper media filter with high gas flow rate being maintained by a large capacity 180m^3/h pumping system. Gas temperature is controlled using a water-cooled heat exchanger in the gas stream (intercooler). Positioning control of the laser beam is achieved using a 16-bit digital scanning system providing spatial positioning and temporal control. All data to drive the process is produced using QuantAM (Renishaw, UK), a standard AM file production software system which takes STL input producing MTT control files in the usual manner. The MTT control files produced are subsequently handled on the machine by a laser scheduling and control system which splits the MTT file producing data streams to control each channel of the machine. This architecture allows standard commercially available build setup software to drive any number of lasers.

The characteristics described above are essential for the successful implementation of multi-laser L-PBF, and the attainment of these consistent process conditions for the application of multi-laser L-PBF must not be underestimated. The remainder of the machine characteristics are of little consequence in this study and hence the reader is directed to reference [7] should further information be required.

2.2 Single- and Multi-Laser Selective Melting Arrangement

Two different L-PBF arrangements were involved in this study. Unlike in the single-laser powder bed fusion (L-PBF)

setup, the multi-laser configuration has each specimen produced with an individual laser directed to it, this is the so-called single-multi-laser powder bed fusion (SM-L-PBF) mode. Table 1 gives details of the arrangements and Fig. 1 depicts the two different laser paths involved.

2.3 Specimen Type and Build Configuration

Two types of specimen were manufactured to investigate the influence of the two laser arrangements, i.e. L-PBF and SM-L-PBF, on mechanical properties. They are the 10 mm × 10 mm × 10 mm cubes and Ø 14 mm × 100 mm cylinders, hereafter referred to as cubes and cylinders. Table 2 describes the specimen types and the mechanical testing which they are designed for, whilst Fig. 2 depicts the build configuration of specimens across the L-PBF machine processing area.

2.4 Feedstock Powder

The IN625 powder used for both L-PBF and SM-L-PBF is standard gas atomised powder material supplied by Renishaw with characteristics indicated in Table 3.

2.5 Process Optimisation

Process optimisation was conducted on In718 and transferred to In625 for this study. The process window was identified by building 10 mm × 10 mm × 10 mm cubes and evaluating their optical density. Subsequently, a half-factorial design of experiments (DOE) methodology was used to optimise the process window. The DOE was developed in Minitab® 17 (Minitab Inc., USA) over four process variables; power, point distance, exposure time, and hatch distance, in accordance with the Renishaw DOE manual.

2.6 Heat Treatment

L-PBF manufactured components suffer from thermal residual stress [9] and annealing was carried out to relieve the stress [10]. AB cubes and cylinders form L-PBF and SM-L-PBF builds were heat-treated in a vacuum furnace at 1048 ± 10 °C for 60 min, with a heating rate of 9 °C/min under 1 × 10^{-4} mbar to 1 × 10^{-6} mbar. The holding time was in accordance with industrial common practice of 1 h per inch of maximum cross section [11]. HT specimens were then cooled in the furnace to room temperature at 1 bar argon gas pressure.

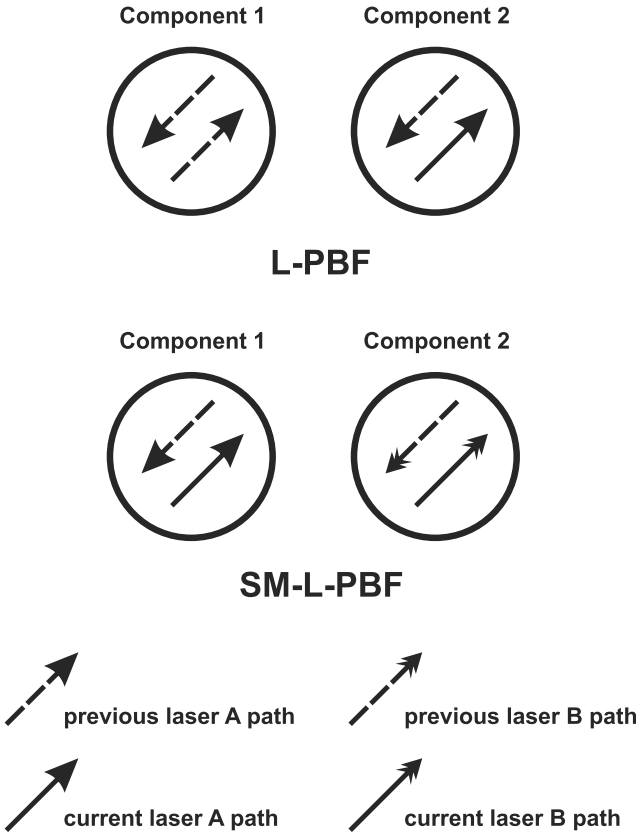

Fig. 1 L-PBF and SM-L-PBF laser paths schematic

2.7 Automated Polishing

To facilitate rapid and consistent production of specimens, automated polishing was used. AB and HT cubes from L-BPF and SM-L-PBF were automatically polished using a Buehler Automet™ 250 grinder polisher (Buehler, USA) to 20 nm surface finish with the use of non-crystallising colloidal silica.

2.8 Optical Density Testing

Optical density testing was carried out on AB and HT cubes from L-PBF and SM-L-PBF by inspection using a SmartScope® ZIP 300 (OGP, UK) optical CMM. Twenty images of each cube were taken, stitched together, threshold applied to generate binary images, and pixel counted to reveal the metallurgical porosity of the specimens. This method is able to detect pores of 14 μm in diameter.

Table 1 The two different L-PBF arrangements involved in this study

Arrangement	Number of lasers	Laser type(max. power)	Wavelength (λ)
L-PBF	1	200 W, modulated (500 W)	1070 nm
SM-L-PBF	4	200 W, modulated (500 W)	1070 nm

Table 2 Specimen type and corresponding mechanical testing

Specimen type	Mechanical Testing
10 mm × 10 mm × 10 mm cube	Optical density, Vickers hardness, microstructure
Ø 14 mm × 100 mm cylinder	Tensile

2.9 Microstructure Evaluation

Electron backscattered diffraction (EBSD) allows the measurement of the crystal orientation and grain size of the specimens. An AB and HT cube from L-PBF and SM-L-PBF were examined in three principle directions, i.e. the XY, XZ and YZ planes, with the Z direction being the L-PBF build direction. Specimens were prepared with standard metallographic methods, including auto-grinding and auto-polishing. Hot mounting with conductive resin was carried out on the specimens following polishing. EBSD measurements were performed using a Helios 600i NanoLab ™ (FEI Company, USA), dual FIB/SEM equipped with a DigiView ™system (EDAX, USA) and Orientation Imaging Microscopy (OIM) data collection and analysis software (EDAX, USA). Specimens were tilted to 70° to the incident beam and measurements were recorded using an acceleration voltage of 20 kV, 5.5 nA beam current and step size of 5 μm.

2.10 Tensile Testing

Tensile testing was carried out on AB and HT cylinders from L-PBF and SM-L-PBF in accordance with the ASTM standard E8/E8M [12], using an Instron® 5984 tensile testing machine (Instron, USA) equipped with a UKAS calibrated 100 kN load cell and an Instron® extensometer (Instron, USA). The Ø 14 mm × 100 mm cylinders were machined down to Ø 6 mm × 100 mm and tests were conducted using strain rates of 0.005 min^{-1} (start to yield point) and 0.05 min^{-1} (yield point to failure) with the experiments being logged and controlled using the Bluehill® 3.76 software (Instron, USA).

2.11 Vickers Hardness Testing

Vickers hardness testing was carried out on the polished AB and HT cubes from L-PBF and SM-L-PBF builds in accordance with ASTM standard E92 [13] using a Wilson® VH3100 (Buehler, USA) semi-automatic tester. Indentations were made in a 4 × 3 array into the surface of polished cubes. These indentations were measured using a UKAS calibrated HV0.5 kg load cell and a DiaMet™ (Buehler, USA) hardness testing software.

3 Experimental Results

Experimental data from each of the L-PBF and SM-L-PBF AB and HT specimen sets are presented in the following order: optimised parameters; optical density; microstructure; tensile strength; Vickers hardness.

3.1 Single-Laser Powder Bed Fusion

The following section presents results of AB and HT specimens manufactured by laser powder bed fusion (L-PBF) with a single laser operating alone with no other lasers firing in the machine chamber.

3.1.1 Optimised Parameters

Table 4 gives the L-PBF build parameters and build statistics of the L-PBF build depicted in Fig. 2.

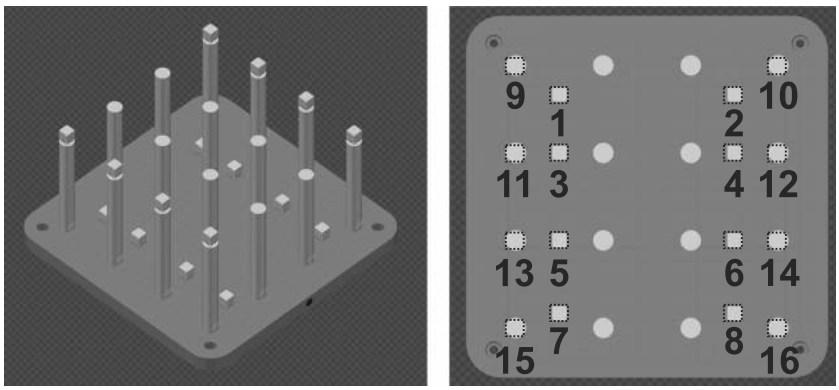

(a) isometric view showing build (b) top view (sample numbers refer to cubes only)

Fig. 2 L-PBF and SM-L-PBF build setup. Build plate dimension is 250 mm × 250 mm. **a** Isometric view showing build, **b** top view (sample numbers refer to cubes only)

Table 3 Characteristics of IN625 powders used in this study [8]

Parameter	Value
Metallic powder	IN625
Chemistry	Nickel balanced, chromium 20 to 23%, molybdenum 8 to 10%, iron < 5%, niobium 3.15 to 4.15%, cobalt < 1%, copper < 0.5%, manganese < 0.5%, silicon < 0.5%, aluminium < 0.4%, titanium < 0.4%, carbon < 0.15%, tantalum < 0.05%, nitrogen < 0.02%, oxygen < 0.02%, phosphorus < 0.015%, sulphur < 0.015%
Bulk density	8.44 g/cm^3
Average tap density	6.17 g/cm^3
Mean size distribution D10	21.8 μm
Mean size distribution D50	32 μm
Mean size distribution D90	46.5 μm

3.1.2 Optical Density

Figure 3 shows the optical density result. It shows no trend in density variation across eight specimens within either AB or HT cubes, or between AB and HT cubes. Both sets have an average specimen bulk density of 99.99% (2 d.p).

3.1.3 Microstructure

Figures 4, 5 and 6 show the EBSD results of L-PBF cubes in the XY, XZ and YZ planes. Figures 4a and b are the unique grain colour maps of the AB and HT XY cubes. Figures 4 c and d are the inverse pole figures of the AB and HT XY cubes. These two plots show that there is a preferred <001> crystallographic orientation parallel to the L-PBF build direction, i.e. the direction of growth. Figures 4e and f are the grain size distributions of the AB and HT XY cubes. These two plots indicate that most of the grain diameters are in the order of 10–100 μm. Figure 5 is the EBSD result for the AB and HT cubes in XZ plane whilst Fig. 6 is that of the YZ plane. Results in these two planes are similar and will be presented together in this paragraph. Figures 5 and 6 a and b are the unique grain colour maps of the AB and HT XZ and YZ cubes. These four figures show that the columnar grains show a preferential growth direction parallel to the L-PBF build direction. Figures 5 and 6 c and d are the inverse pole figures of the AB and HT XZ and YZ cubes. Discrete intensity maxima in the <001> crystallographic orientation can be observed in both north and south poles of the four figures. This observation supports the argument which postulates that the preferential growth direction is parallel to the L-PBF build direction. Figures 5 and 6 e and f are the grain size distributions of the AB and HT XZ and YZ cubes. The two plots indicate that most of the grain diameters are of the order of 10 to 100 μm.

Table 4 Optimised L-PBF build parameters and build statistics

Laser parameters	
Parameter	Value
Powder layer thickness (μm)	30
Peak power (W)	200
Exposure time (μs)	70
Spot size (full-width-half-maximum) (μm)	80
Point distance (μm)	70
Hatch distance (μm)	90
Build statistics	
Parameter	Value
Specimen type	Cube, cylinder
Specimen volume processed (cm^3)	262
Build time (rounded to nearest hour)	52
Build rate (cm^3/h)	5

3.1.4 Tensile Strength

Table 5 and Fig. 7 summarise the tensile behaviour of the L-PBF AB and HT cylinders. The standard error values of the ultimate tensile strength (UTS), 0.2% offset yield strength

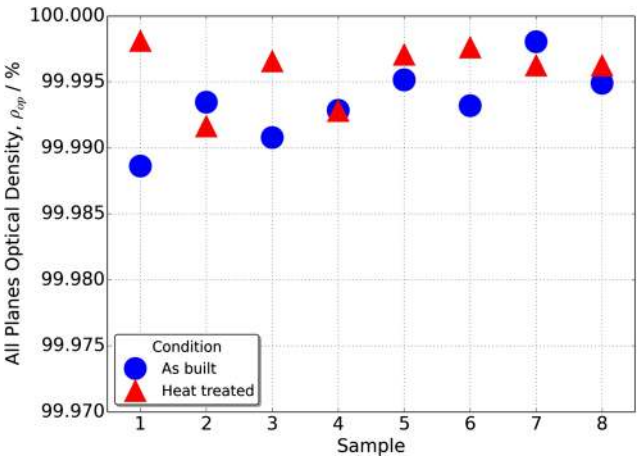

Fig. 3 Optical density of the AB and HT specimens manufactured by L-PBF

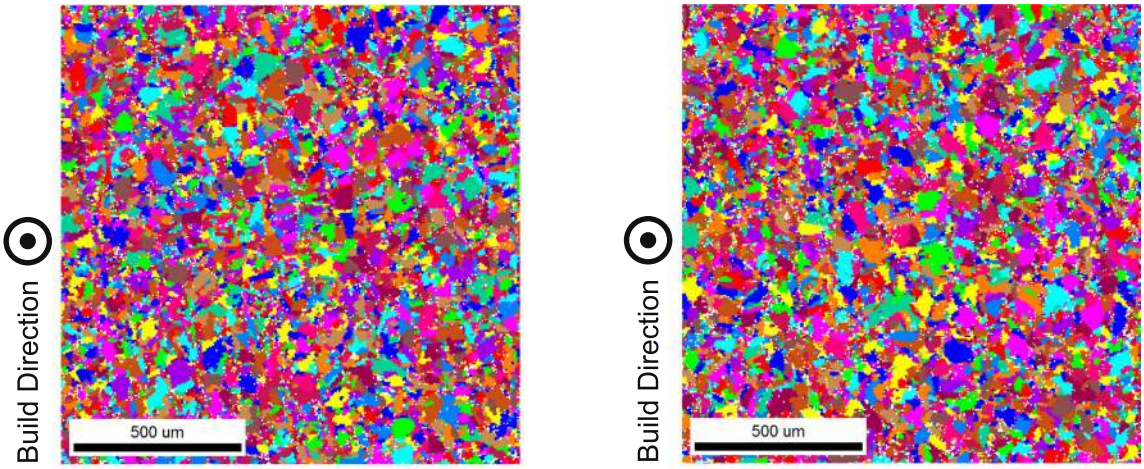

(a) Unique grain colour map, AB (b) Unique grain colour map, HT

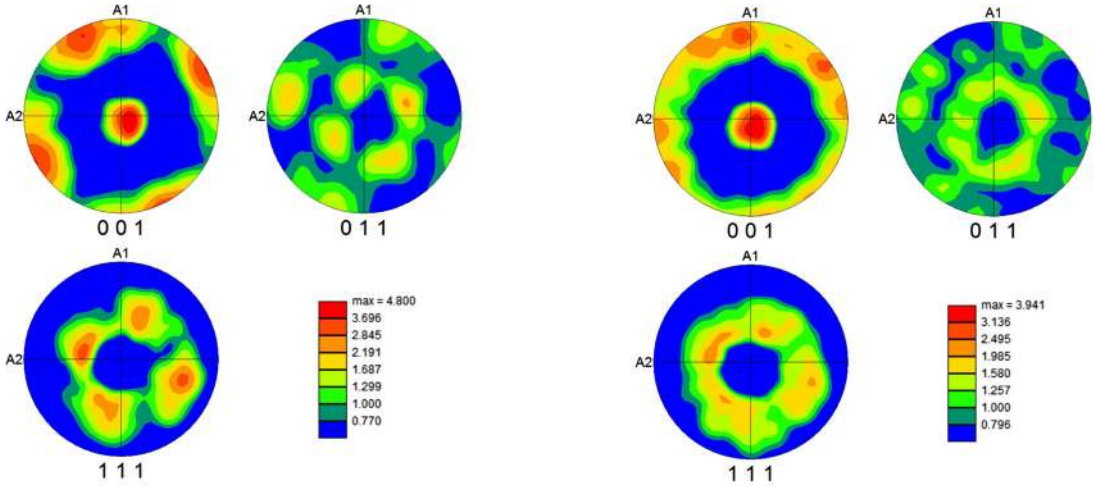

(c) Inverse pole figure, AB (d) Inverse pole figure, HT

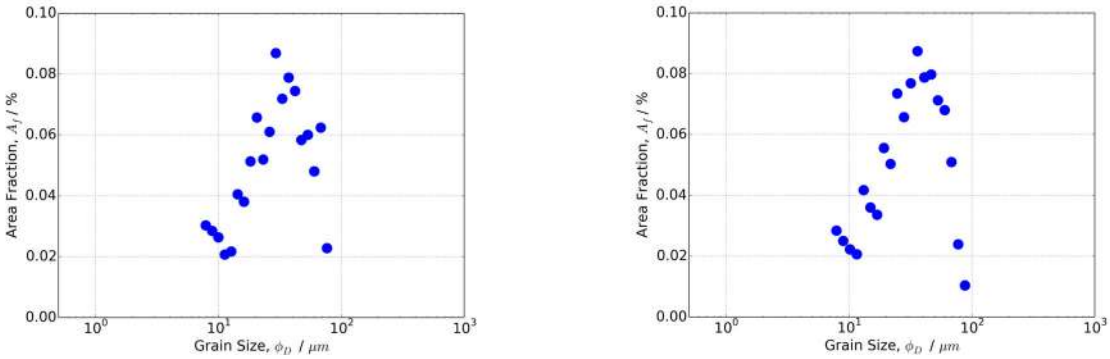

(e) Inverse pole figure, AB (f) Inverse pole figure, HT

Fig. 4 L-PBF EBSD results—XY plane. **a** Unique grain colour map, AB; **b** unique grain colour map, HT; **c** inverse pole figure, AB; **d** inverse pole figure, HT; **e** inverse pole figure, AB; (f) inverse pole figure, HT

(YS) and elongation within both AB and HT sets were insignificant when compared to their average values; this shows that the specimen sets had similar tensile behaviour within each set. Figure 7 depicts that the HT set has lower UTS, lower 0.2% offset YS and greater elongation when compared to those of the AB set.

3.1.5 Vickers Hardness

Figure 8 gives the hardness of the L-PBF AB and HT cubes. The average AB and HT Vickers hardness values were 261.91 HV0.5 (2 d.p) and 269.97 HV0.5 (2 d.p). HV0.5 is the unit in which 0.5 indicates the load used in kgf. Average standard

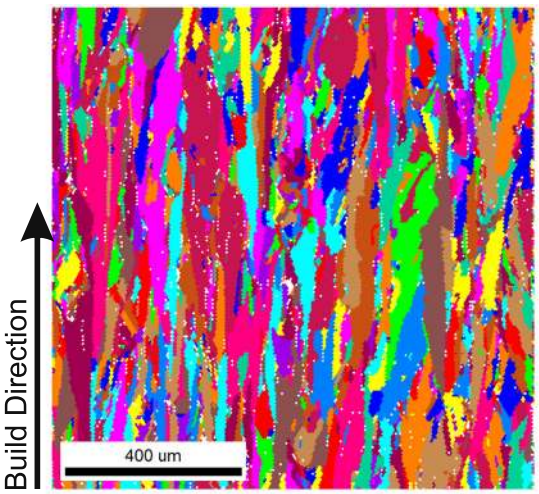

(a) Unique grain colour map, AB

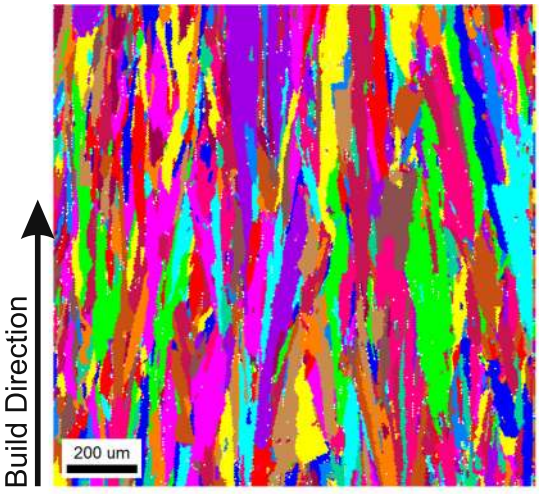

(b) Unique grain colour map, HT

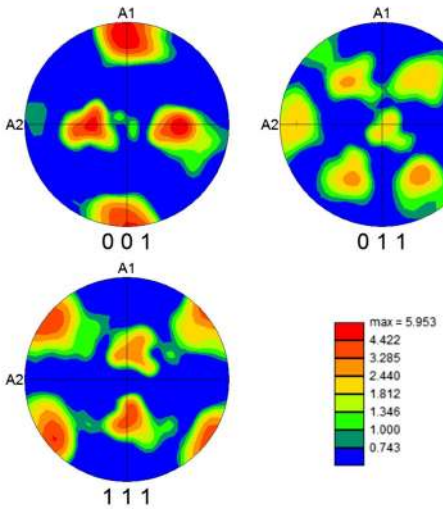

(c) Inverse pole figure, AB

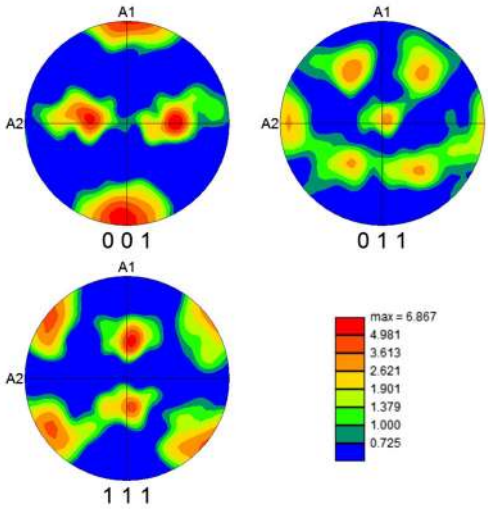

(d) Inverse pole figure, HT

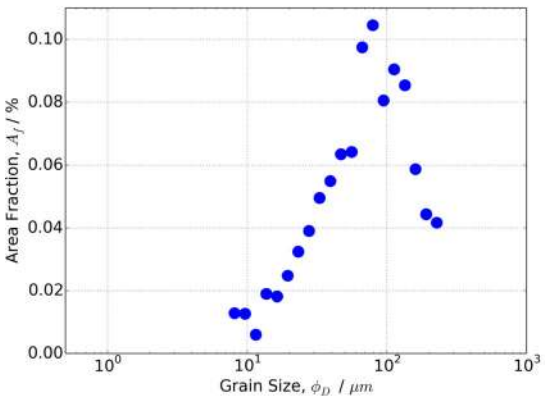

(e) Inverse pole figure, AB

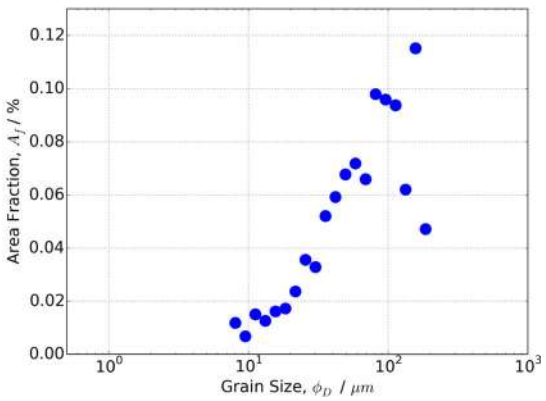

(f) Inverse pole figure, HT

Fig. 5 L-PBF EBSD results—XZ plane. **a** Unique grain colour map, AB; **b** unique grain colour map, HT; **c** inverse pole figure, AB; **d** inverse pole figure, HT; **e** inverse pole figure, AB; **f** inverse pole figure, HT

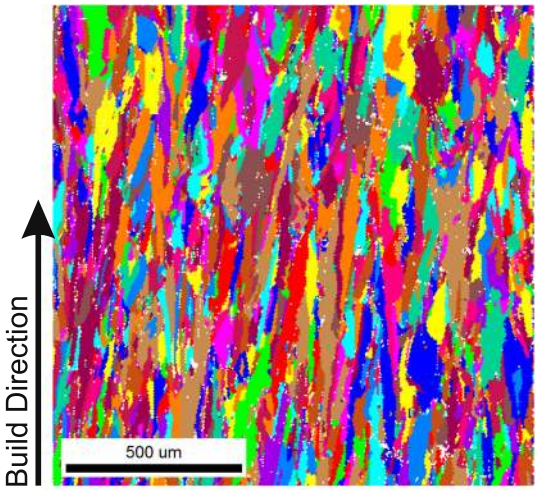

(a) Unique grain colour map, AB

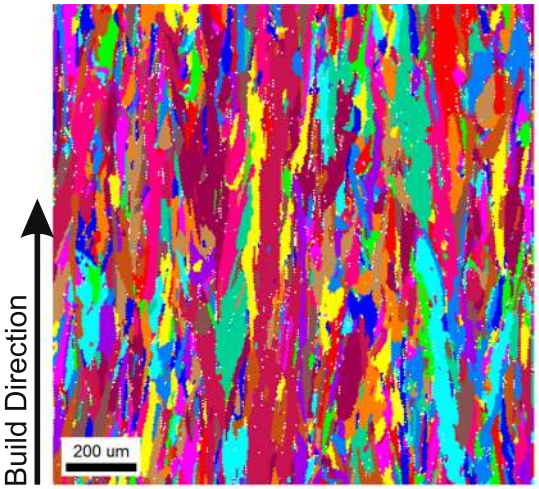

(b) Unique grain colour map, HT

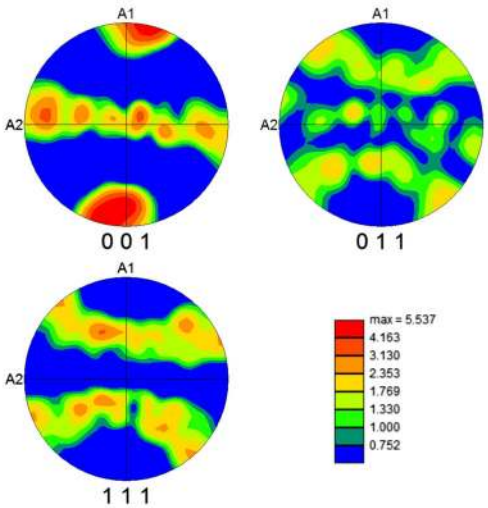

(c) Inverse pole figure, AB

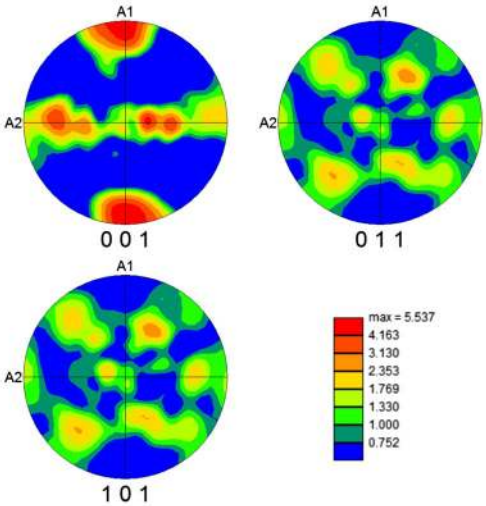

(d) Inverse pole figure, HT

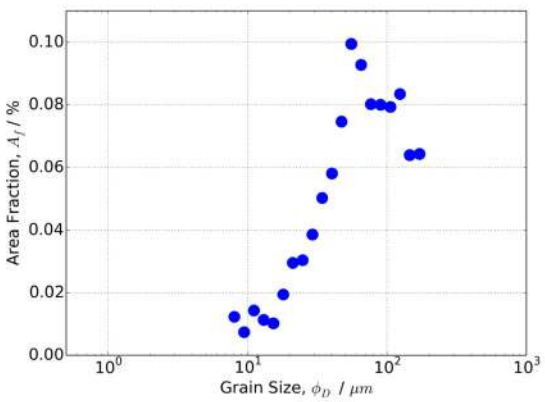

(e) Inverse pole figure, AB

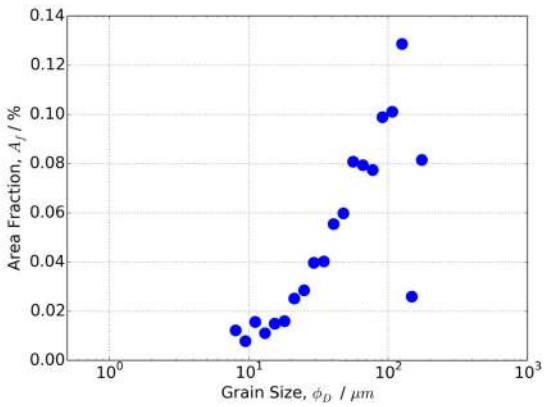

(f) Inverse pole figure, HT

Fig. 6 L-PBF EBSD results—YZ plane. **a** Unique grain colour map, AB; **b** unique grain colour map, HT; **c** inverse pole figure, AB; **d** inverse pole figure, HT; **e** inverse pole figure, AB; **f** inverse pole figure, HT

Table 5 AB and HT specimen average tensile behaviour. Data rounded to 3 s.f

Specimen	UTS/MPa	UTS standard error/MPa	0.2% offset YS/MPa	0.2% offset YS standard error/MPa	Elongation/%	Elongation standard error/%
AB cylinders	901	1.03	619	0.734	56.7	0.0971
HT cylinders	841	0.574	523	0.425	68.5	0.150

error (error bars in plot) calculated for the AB and HT set were 2.77 (2 d.p) and 2.74 (2 d.p). Comparison between AB and HT specimen sets in the figure shows that some specimens have greater hardness after heat treatment.

3.2 Single-Multi Laser Powder Bed Fusion

The following section presents the results of AB and HT specimens manufactured by laser powder bed fusion (L-PBF) with four lasers firing in the machine chamber.

3.2.1 Optimised Parameters

Table 6 gives the SM-L-PBF build parameters and statistics of the SM-L-PBF build depicted in Fig. 2.

3.2.2 Optical Density

Figure 9 shows no trend in density variation across eight specimens within either AB or HT cubes, and between AB and HT cubes. Both sets have an average specimen bulk density of 99.99% (2 d.p).

3.2.3 Microstructure

Figures 10, 11 and 12 show the EBSD results of SM-L-PBF cubes. Figures 10, 11 and 12a and b are the unique grain colour maps of the AB and HT cubes in the XY, XZ and YZ planes. Figures 10, 11 and 12 c and d are the inverse pole figures of the AB and HT cubes in the three planes. These SM-L-PBF results show the same key features as those of the L-PBF described in Section 3.1.3: (1) the <001> crystallographic orientation patterns of the AB/HT XY, XZ and YZ plane datasets indicate that the microstructure has a preferential grain growth direction parallel to the build direction, and (2) the grain diameters are of the order of 10 to 100 μm.

3.2.4 Tensile Strength

Table 7 and Fig. 13 summarise the tensile behaviour of the SM-L-PBF AB and HT cylinders. The standard error values of the UTS, 0.2% offset yield and elongation in both AB and HT sets were insignificant when compared to their average values, this showed that the specimen sets had similar tensile behaviour within each set. Figure 12 depicts that the HT set has lower UTS, lower 0.2% offset YS and greater elongation when compared to those of the AB set.

3.2.5 Vickers Hardness

Figure 14 gives the hardness of the SM-L-PBF AB and HT cubes. The average AB and HT Vickers hardness values were found to be 284.25 HV0.5 (2 d.p) and 271.08 HV0.5 (2 d.p). Average standard error (error bars in plot) calculated for the AB and HT set were 2.35 (2dp) and 2.25 (2 d.p). Comparison

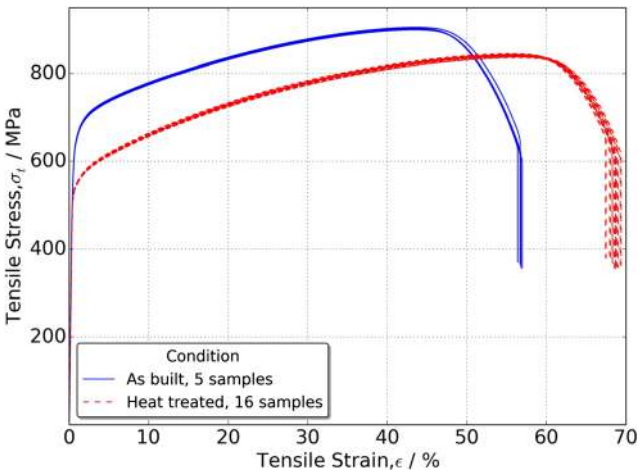

Fig. 7 Tensile strength of the AB and HT specimens manufactured by L-PBF

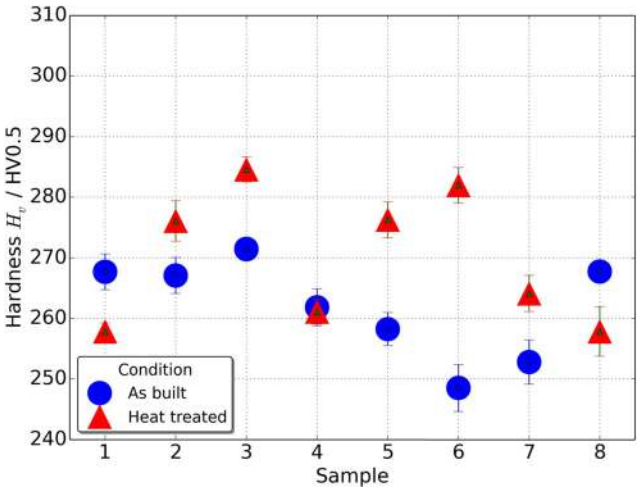

Fig. 8 Vickers hardness of the AB and HT specimens manufactured by L-PBF

Table 6 Optimised SM-L-PBF build parameters and build statistics

Laser parameters	
Parameter	Value
Powder layer thickness (μm)	30
Peak power (W)	200
Exposure time (μs)	70
Spot size (full-width-half-maximum) (μm)	80
Point distance (μm)	70
Hatch distance (μm)	90
Build statistics	
Parameter	Value
Specimen type	Cube, cylinder
Specimen volume processed (cm^3)	262
Build time (rounded to nearest hour)	19
Build rate (cm^3/h)	14

between AB and HT specimen sets in the figure shows a general reduction in hardness after heat treatment.

4 Discussion

In this section, analyses on mechanical properties for the L-PBF and SM-L-PBF, AB and HT specimen sets are made. Comparisons between L-PBF and SM-L-PBF are only made on HT specimens as only stress-relieved components are used in commercial applications with IN625.

4.1 Optical Density

The four L-PBF/SM-L-PBF, AB/HT datasets have an average specimen density of 99.99% (2 d.p). Variations in density between the AB and HT sets, in both L-PBF and SM-PBF, are all less than 0.01%, this implies that the heat treatment process carried out in this study did not influence specimen density. The density result achieved in this study is on a par with or exceeds values reported (98.5 to 99.5%) in the literature on L-PBF IN625 specimens [14].

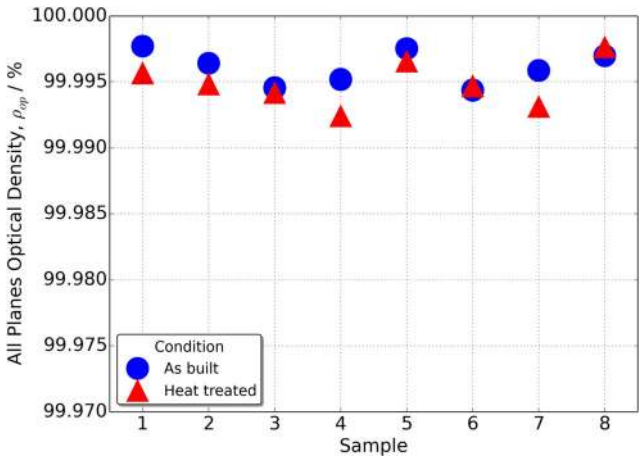

Fig. 9 Optical density of the AB and HT cubes manufactured by SM-L-PBF

4.2 Microstructure

Figures 4, 5 and 6 a–f and Figs. 10, 11 and 12 a–f show that both the stress-relieving heat treatment and the multi-laser arrangements have little to no effect on the microstructure of the specimens. The unique grain colour maps and the inverse pole figures of the XY, XZ and YZ planes in the AB/HT, L-PBF/SM-PBF datasets demonstrate that the preferred crystallographic orientation of columnar grains growth is parallel to the L-PBF build direction. This observation is in line with other experimental results in the literature [15]. Results show that the grain size from the AB/HT, L-PBF/SM-L-PBF datasets is of the order of 10 to100 μm. This grain size range also matches other experimental results reported in the literature [16].

4.3 Tensile Strength

Variation in the standard error values between the four L-PBF, SM-L-PBF, AB and HT data sets were insignificant. This shows that the specimen sets have similar tensile behaviour within each set. The cylinders were built in the configuration described in Fig. 2. The build layout and the low CV values indicate that the specimen tensile strength is independent of build location across the machine processing area. Figure 7 depicts that the L-PBF HT set has lower UTS, lower 0.2% offset YS and greater elongation when compared to those of the L-PBF AB set. It is thought that these HT cylinders were more ductile when compared to the AB cylinders. Similar to the tensile behaviour in L-PBF, Fig. 13 depicts that the SM-L-PBF HT set also has lower UTS, lower 0.2% offset YS and greater elongation when compared to those of the SM-L-PBF AB set.

The increase in ductility is attributed to the heat treatment process carried out in this study. L-PBF manufactured specimens suffer from thermal residual stress and melted areas were plastically deformed and work-hardened under stress [17, 18]. Heat treatment relieves thermal residual stress. Thus, HT cylinders are easier to deform when compared to AB cylinders. This results in greater strain under the same level of stress, lower UTS, 0.2% offset YS and greater elongation before fracture, when compared to AB cylinders.

Table 8 is compiled by drawing data from Tables 5 and 7 and both ASTM B564 and B446 standards [19, 20]. Results show that the tensile behaviour of L-PBF HT and SM-L-PBF HT cylinders are comparable. The percentage differences on UTS, 0.2% YS and elongation and between the L-PBF HT and SM-L-PBF HT cylinders are 1.7%, 3.2% and 1.2%

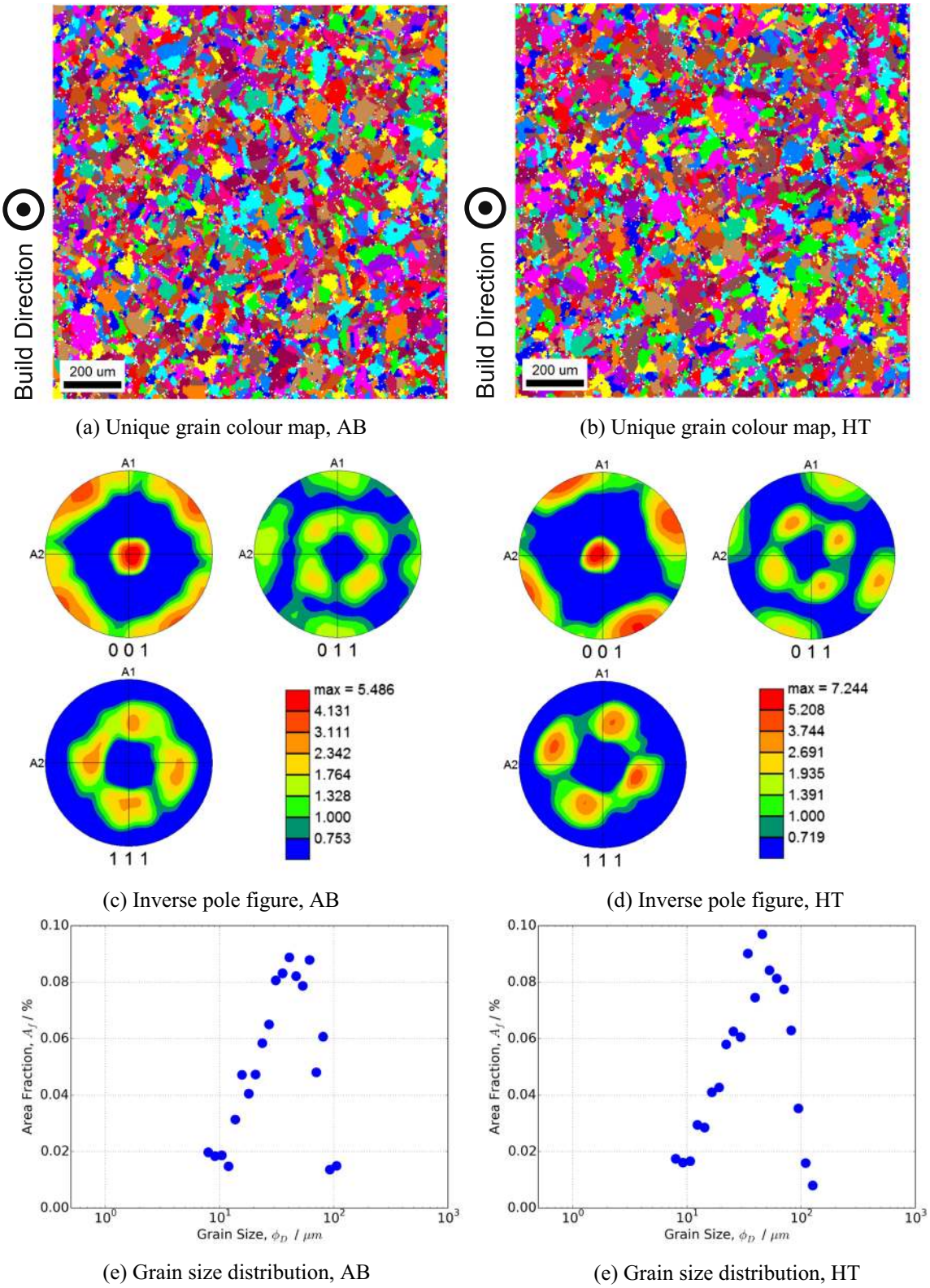

(a) Unique grain colour map, AB

(b) Unique grain colour map, HT

(c) Inverse pole figure, AB

(d) Inverse pole figure, HT

(e) Grain size distribution, AB

(e) Grain size distribution, HT

Fig. 10 SM-L-PBF EBSD results—XY plane. **a** Unique grain colour map, AB; **b** unique grain colour map, HT; **c** inverse pole figure, AB; **d** inverse pole figure, HT; **e** grain size distribution, AB; **f** grain size distribution, HT

respectively. Although only by a small margin, SM-L-PBF HT cylinders appear to have lower UTS and 0.2% offset YS, and greater elongation when compared to L-PBF HT cylinders. This suggests that the L-PBF cylinders had greater

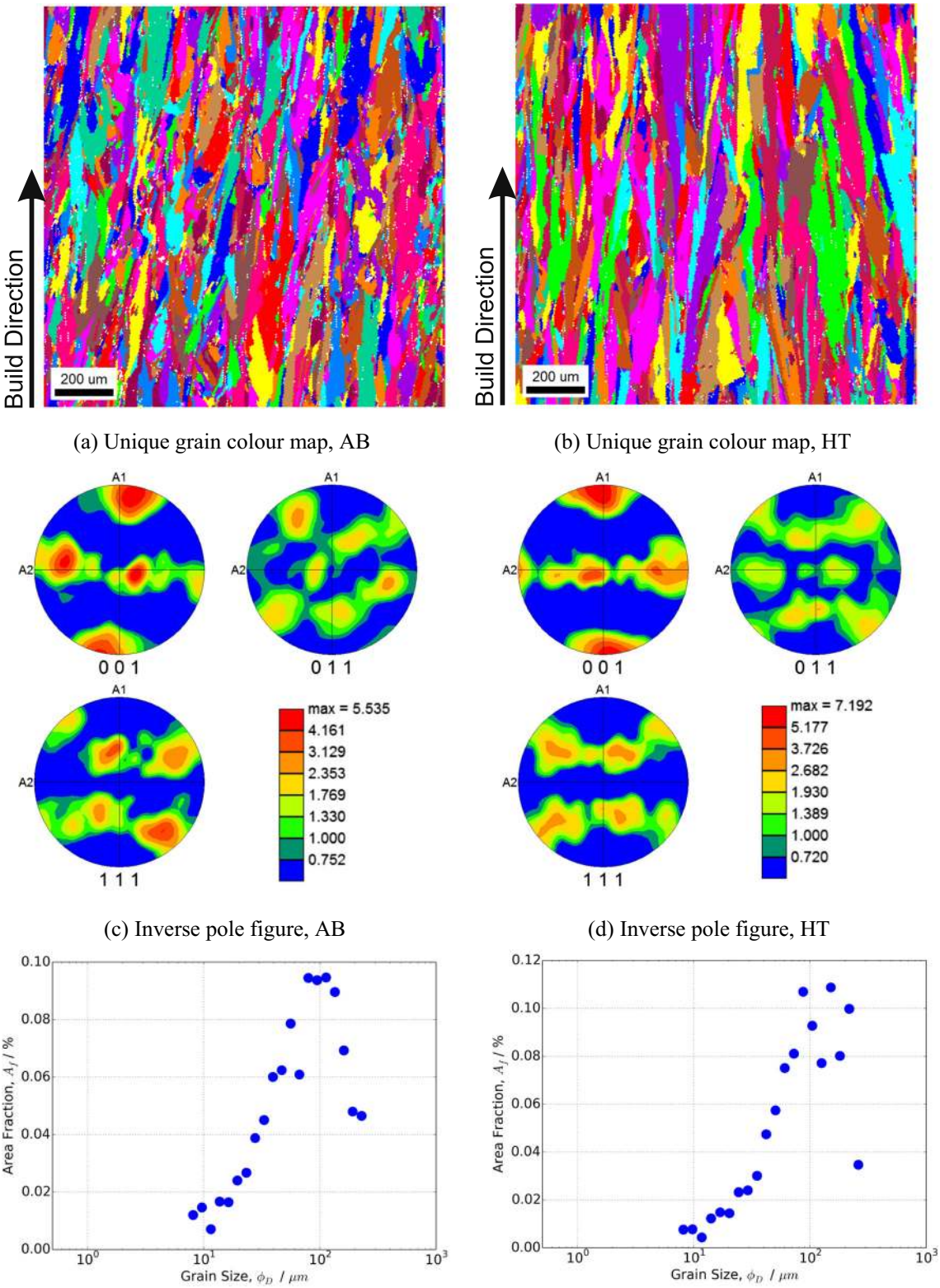

(a) Unique grain colour map, AB

(b) Unique grain colour map, HT

(c) Inverse pole figure, AB

(d) Inverse pole figure, HT

(e) Inverse pole figure, AB

(f) Inverse pole figure, HT

Fig. 11 SM-L-PBF EBSD results—XZ plane; **a** Unique grain colour map, AB; **b** unique grain colour map, HT; **c** inverse pole figure, AB; **d** inverse pole figure, HT; **e** inverse pole figure, AB; **f** inverse pole figure, HT

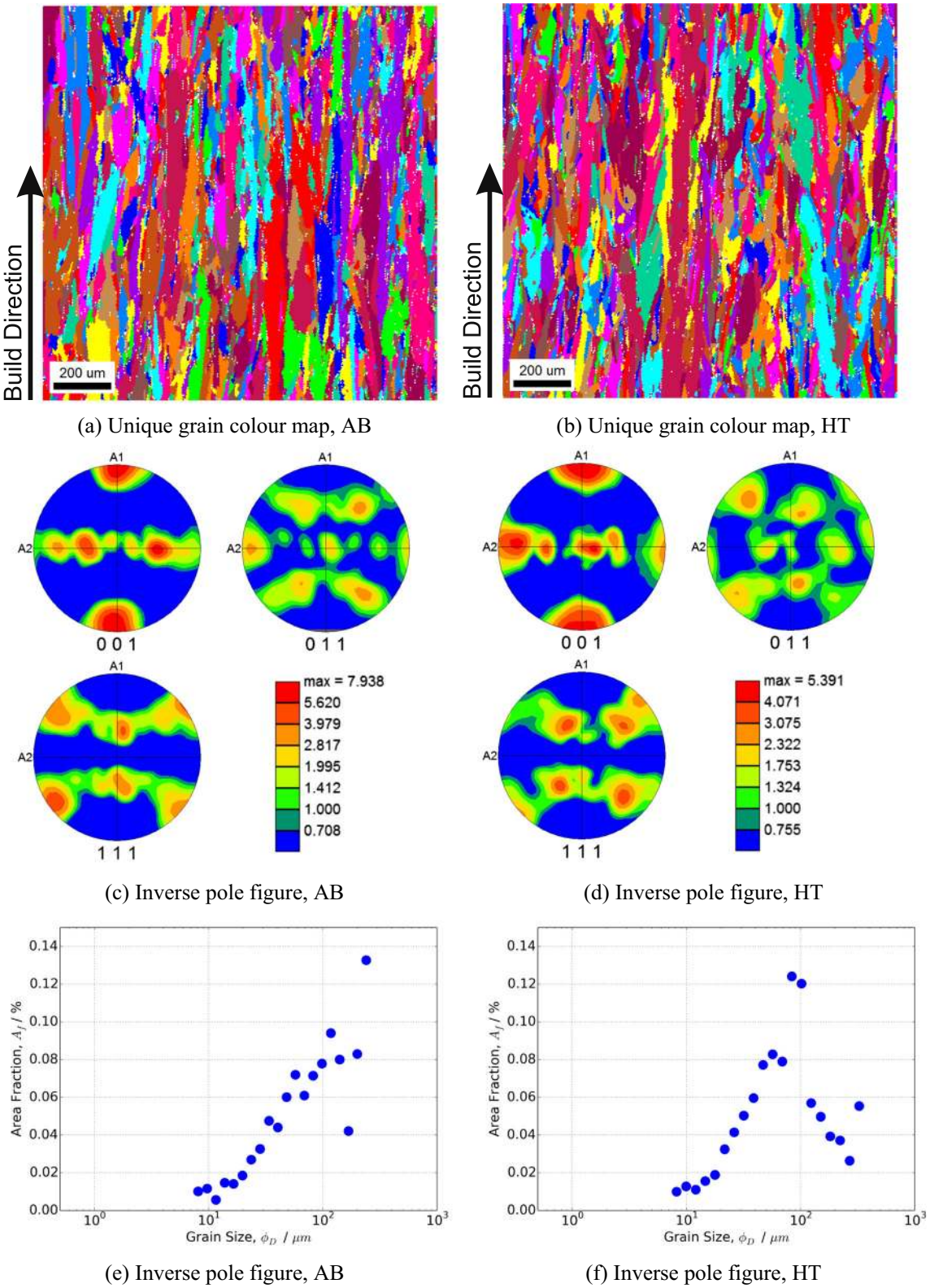

(a) Unique grain colour map, AB

(b) Unique grain colour map, HT

(c) Inverse pole figure, AB

(d) Inverse pole figure, HT

(e) Inverse pole figure, AB

(f) Inverse pole figure, HT

Fig. 12 SM-L-PBF EBSD results—YZ plane. **a** Unique grain colour map, AB; **b** unique grain colour map, HT; **c** inverse pole figure, AB; **d** inverse pole figure, HT; **e** inverse pole figure, AB; **f** inverse pole figure, HT

residual tensile stress. As the average processed layer time in a L-PBF build is greater than that of a SM-L-PBF build, the time interval for any component to be worked by the laser is greater in L-PBF. This is believed to have led to a longer

Table 7 AB and HT specimen average tensile behaviour. Data are rounded to 3 s.f

Specimen	UTS/MPa	UTS standard error/MPa	0.2 % offset YS standard error/MPa	Offset YS standard error/MPa	Elongation/%	Elongation standard error/%
AB cylinders	864	0.700	585	0.393	58.6	0.100
HT cylinders	827	0.726	507	0.493	69.3	0.0750

cooling time between layers for the L-PBF cylinders. Moreover, Table 8 also shows that L-PBF and SM-L-PBF HT cylinders tensile properties either meet or exceed the tensile requirements set out by ASTM standards on IN625 components manufactured by conventional methods.

4.4 Vickers Hardness

All cubes from the four L-PBF/SM-L-PBF and AB/HT datasets involved in hardness test underwent 12 hardness measurements on the Vickers hardness machine. The average standard error (error bar in Figs. 8 and 14) of all four datasets is less than 2.8%. The low standard error values imply that the hardness measurements are consistent.

Figure 8 shows that L-PBF/SM-L-PBF AB and HT cubes have similar hardness. The maximum difference in hardness between the L-PBF/SM-L-PBF AB and HT cube is less than 7%. Results also show that the hardness property of L-PBF HT and SM-L-PBF HT cubes are comparable, the difference in their average Vickers hardness is less than 1% (data from Sections 3.1.5 and 3.2.5). In addition, the average hardness achieved in this study is in the same order, 280HV0.5, of that reported in literature on L-PBF nickel alloy specimens [21].

When compared to the AB/HT SM-L-PBF dataset (Fig. 14), the AB/HT L-PBF dataset (Fig. 8) shows that the hardness values scatter more across the eight cube samples. Figure 2 shows that cube 1 to 8 were built directly on the build plate alongside the cylinders, whilst cubes 9 to 16 were built on top of the cylinders. The inter-layer laser melting time interval for cubes 1 to 8 was different from that of cubes 9 to 16, as there were 24 components to process when cubes 1 to 8 were manufactured (8 cubes and 16 cylinders) whilst there were only 8 to process when cube 9–16 were manufactured (8 cubes only). Although this situation was the same for both L-PBF and SM-L-PBF, the inter-layer time interval was less in SM-L-PBF as there were four material processing lasers. It is thought that the greater time interval in L-PBF might have played a role affecting the hardness in the cubes, leading to greater variation when compared to that of the SM-L-PBF dataset.

4.5 Build Rate

Results show that, for an IN625 build at 30-μm layer thickness, the build rate of SM-L-PBF arrangement is 14 cm^3/h whilst that of the L-PBF is 5 cm^3/h. The SM-L-PBF build rate is 2.74 times higher, and the production time saved due to the high throughput of the SM-L-PBF system is 63% (Tables 4 and 6). In this study, there are four lasers in the SM-L-PBF mode and one in L-PBF. Although laser melting can be conducted more effectively with the multi-laser arrangement, the time consumed in the powder deposition step stays the same. The proportion of powder deposition time in the total build

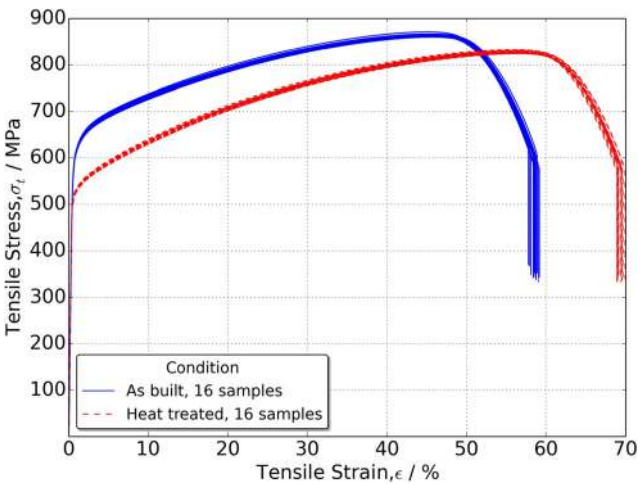

Fig. 13 Tensile strength of the AB and HT specimens manufactured by SM-L-PBF

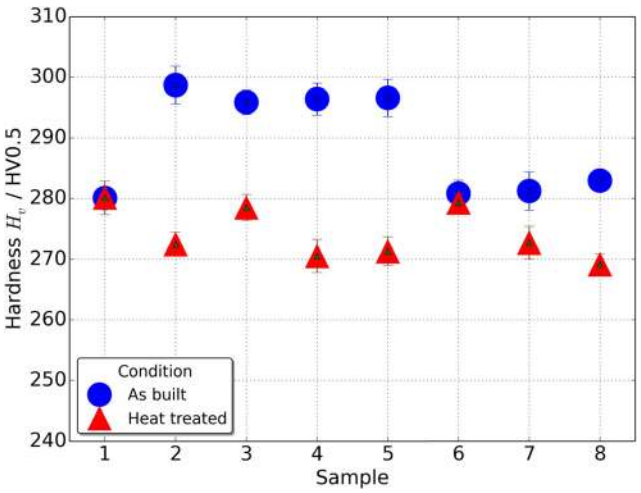

Fig. 14 Vickers hardness of the AB and HT specimens manufactured by SM-L-PBF

Table 8 Results against ASTM standards on tensile requirements. Data rounded to 3 s.f

Specimen	UTS/MPa	0.2% offset YS/MPa	Elongation/%
L-PBF HT cylinders	841	523	68.5
SM-L-PBF HT cylinders	827	507	69.3
ASTM requirements (B564, B446)	827	414	30.0

time in this study was particularly significant, as a thin powder layer of 30-μm thickness was used. As a result, the reduction in build time observed is less than the expected 75%.

It should be noted that metal AM build rate is material and processing parameter dependent. For example, the RenAM500Q machine build rate reported in this study is 14cm^3/h when four 200 W lasers were used to process IN625 at a layer thickness of 30 μm (Table 6). On another occasion, when processing AlSi10Mg with four 500 W lasers at a layer thickness of 60 μm, the build rate achieved was 77 cm^3/h [22] (the RenAM 500Q is capable of achieving 150 cm^3/h [23]). Moreover, this study does not aim to showcase the maximum material processing speed of the SM-L-PBF arrangement, but to demonstrate: (1) the fine control on mechanical properties through an optimised build parameter set, and (2) the increase in build rate of the SM-L-PBF arrangement when compared to that of the L-PBF.

5 Conclusions

IN625 specimens have been manufactured using a RenAM500Q machine with L-PBF and SM-L-PBF options. Stress-relieving heat treatment was carried out on half of the specimens. Optical density, microstructure, tensile behaviour and Vickers hardness of all laser configuration AB and HT specimens were evaluated. Results show that the SM-L-PBF system achieved a build rate of 14 cm^3/h when processing IN625 at a powder layer thickness of 30 μm. The increase in build rate when compared to that of L-PBF is 2.74 times without compromising the mechanical behaviour and microstructure of the specimens. The stress-relieving heat treatment improves ductility of specimens across the board without compromising density or changing microstructure markedly. For all four L-PBF/SM-L-PBF and AB/HT datasets, average specimen density is above 99.99%, which is on par with or exceed the value reported in literature [14]. Average tensile behaviour including UTS, 0.2% offset YS and elongation all exceeds ASTM requirements for IN625 specimens [19, 20]. Average specimen hardness and grain size are in the same order of that reported in literature (280HV0.5 [21], 10 to100 μm [16]).

This study has addressed the research gaps by proposing an experimental design to benchmark the efficiency of a multi-laser system, and demonstrating that the mechanical properties of specimens are not compromised when each specimen was manufactured by a single laser. Nevertheless, this may not be the case where multiple lasers are directed to melt individual specimen, thus more in-depth follow-up studies are required. This study has demonstrated that a multi-laser AM system opens up opportunities to tackle the impasse of low build rate in L-PBF in an industrial setting.

Funding information This work was supported by the EPSRC Centre for Innovative Manufacturing in Laser-based Production Processes (grant number EP/K030884/1).

Open Access This article is distributed under the terms of the Creative Commons Attribution 4.0 International License (http://creativecommons.org/licenses/by/4.0/), which permits unrestricted use, distribution, and reproduction in any medium, provided you give appropriate credit to the original author(s) and the source, provide a link to the Creative Commons license, and indicate if changes were made.

References

1. Bhavar V, Kattire P, Patil VM, Khot SM, Gujar K, Singh RR (2017), Additive Manufacturing Handbook, Chapter 15: A review on powder bed fusion technology of metal additive manufacturing, Taylor & Francis Group, https://doi.org/10.1201/9781315119106-15
2. Ford S, Despeisse M (2016) Additive manufacturing and sustainability: an exploratory study of the advantages and challenges. J Clean Prod 137:1573–1587. https://doi.org/10.1016/j.jclepro.2016.04.150
3. Gokuldoss PK, Kolla S, Eckert J (2017) Additive manufacturing processes: selective laser melting, electron beam melting and binder jetting—selection guidelines. Materials 10:672. https://doi.org/10.3390/ma10060672
4. Milewski JO (2017) Additive manufacturing of metals: from fundamental technology to rocket nozzles, medical implants, and custom jewelry, Springer, ISSN 2196-2812, pp. 90-98
5. Andani MT, Dehghani R, Karamooz-Ravari MR, Mirzaeifar R, Ni J (2017) Spatter formation in selective laser melting process using multi-laser technology. Elsevier Mater Des 131:460–469. https://doi.org/10.1016/j.matdes.2017.06.040
6. Li F, Wang Z, Zeng X (2017) Microstructures and mechanical properties of Ti6Al4V alloy fabricated by multi-laser beam selective laser melting. Elsevier Mater Lett 199:79–83. https://doi.org/10.1016/j.matlet.2017.04.050
7. Renishaw RenAM 500Q multi-laser AM system specification and data sheet https://www.renishaw.com/en/renam-500q%2D%2D42781

8. Renishaw In625-0402 powder for additive manufacturing https://resources.renishaw.com/en/details/data-sheet-in625-0402-powder-for-additive-manufacturing%2D%2D97039
9. Mercelis P, Kruth JP (2006) Residual stresses in selective laser sintering and selective laser melting. Rapid Prototyp J 12(5):254–265. https://doi.org/10.1108/13552540610707013
10. Losertová M, Kubeš V (2017) Microstructure and mechanical properties of selective laser melted Ti6Al4V Alloy. IOP Conf Series: Materials Science and Engineering 266(2017):012009. https://doi.org/10.1088/1757-899X/266/1/012009
11. The Pennsylvania State University, Heat treatment procedure qualification, final technical report work performed under contract no. DE-FC07-99ID13841, Work Prepared for U.S. Department of Energy
12. ASTM E8/E8M Standard test methods for tension testing of metallic materials
13. ASTM E92-82 Standard test methods for Vickers hardness of metallic materials
14. Spierings AB, Bauer T, Dawson K, Collella A, Wegener K (2015) Processing ODS modified In625 using selective laser melting, Proceedings from the Solid Freeform Fabrication Symposium
15. Bauer T, Dawson K, Spierings AB, Wegener K (2015) Microstructure and mechanical characterisation of SLM processed Haynes ® 230 ®, Proceedings from the Solid Freeform Fabrication Symposium
16. Lia C, Whiteb R, Fangc XY, Weaverb M, Guoa YB (2017) Microstructure evolution characteristics of Inconel 625 alloy from selective laser melting to heat treatment. Mater Sci Eng A 705:20–31. https://doi.org/10.1016/j.msea.2017.08.058
17. Robinson J (2014) Optimisation of the selective laser melting process for the production of hybrid orthopaedic devices, PhD Thesis, The University of Liverpool, pp. 42-50, 113-161
18. Mukasyan A, Chapter 7 Dislocations and strengthening mechanisms, teaching materials, CBE 30361 Science of Engineering Materials, University of Notre Dame
19. ASTM B564 Standard specification for nickel alloy forgings
20. ASTM_B446 Standard specification for nickel-chromium-molybdenum-columbium alloy (UNS N06625), nickel-chromium-molybdenum-silicon alloy (UNS N06219), and nickel-chromium-molybdenum-tungsten alloy (UNS N06650) rod and bar
21. Harrison NJ (2016) Selective laser melting of nickel superalloys: solidification, microstructure and material response, PhD Thesis, The University of Sheffield, Faculty of Engineering, School of Mechanical Engineering, pp. 203
22. C. Martell (2018) The Renishaw additive manufacturing formula, Presentation Materials at the Renishaw Investor Day, http://resources.renishaw.com/en/download/presentation-investor-day-2018-additive-manufacturing%2D%2D102128
23. Renishaw RenAM 500 series additive manufacturing system data sheet, https://www.renishaw.com/en/renam-500q%2D%2D42781

Publisher's note Springer Nature remains neutral with regard to jurisdictional claims in published maps and institutional affiliations.